Effect of lignin incorporation on the performance of epoxidized soybean oil biobased coatings for corrosion protection

Progress in Organic Coatings 214 (2026) 110024

Contents lists available at ScienceDirect

Progress in Organic Coatings

journal homepage: www.elsevier.com/locate/porgcoat

Effect of lignin incorporation on the performance of epoxidized soybean oil biobased coatings for corrosion protection

Saba Moradi Boldaji [a], Leonardo Iannucci [a,*], Sabrina Grassini [a], Luca Carlomaria Pariani [c], Letizia Anna Maria Rossato [c], Paola D'Arrigo [c,d], Camilla Noè [a,*], Massimo Messori [a,b]

[a] Department of Applied Science and Technology, Politecnico di Torino, Torino, 10129, Italy
[b] National Interuniversity Consortium of Materials Science and Technology (INSTM), Via G. Giusti 9, 50121, Firenze, Italy
[c] Department of Chemistry, Materials and Chemical Engineering "Giulio Natta", Politecnico di Milano, p.zza Leonardo da Vinci 32, Milano, 20133, Italy
[d] Istituto di Scienze e Tecnologie Chimiche "Giulio Natta", Consiglio Nazionale delle Ricerche (SCITEC-CNR), via Luigi Mancinelli 7, Milano, 20131, Italy

ARTICLE INFO

Keywords:
Lignin
Bio-Based Resins
Cationic UV-curing
Corrosion-Resistant Coatings

ABSTRACT

This study reports a fully bio-based, UV-cured anti-corrosion coating developed by mixing epoxidized soybean oil (ESO) and lignin. Rheology and photorheology revealed stable viscosity and high UV reactivity, while Fourier Transform Infrared spectroscopy showed high epoxy group conversion. The coatings exhibited robust thermal stability (as determined by thermogravimetric analysis) and valuable surface properties, including high pencil hardness, excellent adhesion, good solvent resistance, and tunable contact angle. Electrochemical impedance spectroscopy measurements acquired in 3.5 wt%. NaCl electrolyte demonstrated that lignin remarkably improves barrier protection, whereas unmodified ESO films offer little protection against corrosion in a harsh saline environment. Field Emission Scanning Electron Microscopy analysis of coated steel after corrosion tests further confirmed the good corrosion resistance of the coatings. These findings demonstrate a sustainable route to high-performance, eco-friendly corrosion protection.

1. Introduction

Corrosion of metallic materials, particularly steel, remains a significant challenge across various industries, including infrastructure, energy, and transportation, resulting in substantial economic losses, safety risks, and environmental impacts [1]. Organic coatings are among the most widely adopted protection strategies, as they form effective barriers between metal surfaces and corrosive environments [2–6]. At the same time, growing concerns about sustainability and human health have increased the interest in bio-based coatings made from renewable resources. Petroleum-based epoxy resins dominate the thermosetting polymer market, constituting over 60% of global epoxy resin production used in protective coatings. As a result, bio-based thermosets offer a promising path for innovation. Recently, efforts have focused on creating eco-friendly coatings that tackle environmental issues while providing effective corrosion resistance. In this context, designing organic coatings from bio-based oils with good anticorrosion properties has become a key area of research focus [7].

Epoxidized soybean oil (ESO) is industrially synthesized by reacting soybean oil with hydrogen peroxide. Soybean oil, with an estimated production of 66 million tons in 2025 [8], has been widely studied in research as a bio-based polymer building block due to its low cost, high availability and ability to form multi-functional epoxides [9]. Owing to its long hydrophobic chains, ESO exhibits high flexibility and resistance to moisture and chemicals, making it a promising candidate for the development of bio-based anticorrosion epoxy coatings [10]. However, ESO generally requires reinforcement with petroleum or bio-based fillers to improve its mechanical and thermal properties. Various compounds, such as tannic acid [11], gallic acid [12], rosin acid [13], and 2, 5-furan diacrylate [14], have been employed to produce cross-linked ESO-based thermosets with enhanced performance. Additionally, for the same purpose, other green reinforcement sources, such as cellulose nanocrystals and cellulose nanofibers [15], flax fiber [16], and lignin [17] have been evaluated. However, few studies have been conducted on bio-based composites with high bio-epoxy content, highlighting the need for further research.

After cellulose, lignin is the most abundant aromatic biopolymer, originating from plant cell walls and generated in large quantities as a

* Corresponding authors.
E-mail addresses: leonardo.iannucci@polito.it (L. Iannucci), camilla.noe@polito.it (C. Noè).

https://doi.org/10.1016/j.porgcoat.2026.110024
Received 27 November 2025; Received in revised form 29 January 2026; Accepted 2 February 2026
Available online 9 February 2026

by-product of the pulp and paper industry and biorefineries. Nowadays, lignin is usually considered a waste by-product with low residual value. To date, only a small part of the technical lignins produced worldwide is actually used for material manufacturing and chemical synthesis, as the majority is being burnt for energy recovery. Transforming lignin into high-performance materials could not only reduce its low-value use as fuel but also provide a sustainable alternative to petroleum-derived polymers [18]. In addition, lignin has gained attention for protective coatings due to its inherent corrosion-resistant properties, which arise from multiple mechanisms. Indeed, lignin enhances barrier performance by reducing porosity and increasing the tortuosity of diffusion pathways, thereby limiting the ingress of water, oxygen, and chloride ions. Hydroxyl, methoxy, and carboxyl groups further enhance adhesion to metal surfaces, stabilize interfacial layers, and suppress electrochemical activity, thereby improving long-term durability. Phenolic units contribute to antioxidant capacity by neutralizing reactive species and delaying oxidation, whereas their hydrophobic character reduces water and chloride uptake [19].

Recent research has explored the application of lignin on different metallic substrates to assess their effectiveness as sustainable and eco-friendly protective layers [20,21]. They have also explored coating preparation methods and the mechanisms responsible for performance enhancement. For example, Dastpak et al. used organosolv lignin derived from beech (hardwood) and spruce (softwood), dissolved in 1, 4-dioxane, and applied it via spin coating onto stainless steel 316 [22]. The samples were then annealed at 120 °C. Corrosion behavior was evaluated using electrochemical measurements, revealing that the coatings decreased the corrosion rate by up to two orders of magnitude.

Other studies have also explored lignin-based coatings for corrosion protection, but they chose not to use lignin in its natural form, instead opting for various chemical modifications. For example, Lai et al. utilized organosolv lignin to create an anticorrosion coating; however, their production method was quite complex. It involved preparing an emulsion with lignin microspheres grafted with dopamine, which were then mixed with a waterborne petroleum-based epoxy resin. The resulting 80 μm thick coatings exhibited promising corrosion protection [23].

In addition, Wang et al. functionalized organosolv lignin with furan groups through reaction with furfuryl glycidyl ether, producing a lignin-based precursor. This functionalized lignin was then used to develop self-healing coatings through thermal crosslinking with 4, 4′-bismaleimidodiphenylmethane (BMI). The coating solution was applied onto steel substrates using spin coating, followed by a thermal curing at 50 °C for one hour to form a uniform polymeric film and subsequently tested for corrosion protection [24].

Similarly, Diógenes et al. acetylated kraft lignin and incorporated it into a bisphenol A diglycidyl ether resin (DGEBA) system with isophorone diamine, producing anticorrosion films with a thickness of 220 μm after 168 h [25].

While existing research has established the viability of lignin-based coatings for improving corrosion resistance, the synthesis of fully bio-based thermoset composites from lignin presents significant scientific challenges. A significant gap remains in the literature regarding the successful formulation and characterization of such systems, particularly those that effectively integrate multiple bio-derived feedstocks while maintaining the structural integrity, processability, and performance required for industrial applications.

As discussed earlier, soybean oil has shown promising anticorrosion properties, and adding lignin as a reinforcing agent not only can address existing limitations but may also contribute to improved corrosion protection. In this context, Zhou et al. developed fully biobased thermally cured thermosets using multicarboxylated lignin (MGL at 10, 20, and 30 wt% concentration) ESO, and citric acid (CA [17]. However, the study did not examine the corrosion resistance of these composites, leaving a gap in evaluating their full potential for protective coating applications.

In contrast to conventional thermal-curing, the UV-curing process provides an efficient and environmentally-favorable route for developing high-performance protective coatings [26–28,30,31]. This approach offers rapid polymerization at ambient temperature with low energy demand and negligible volatile organic compounds (VOCs) emissions [29]. Therefore, it can be considered more sustainable than thermal curing.

Noè et al. investigated epoxidized vegetable oils (EVOs) as fully bio-based coatings. The formulations used triarylsulfonium hexafluoroantimonate as the photoinitiator and were UV-cured on low-carbon steel substrates, achieving epoxy conversion rates of 93–99. EIS measurements in 0.1 M NaCl after 168 h of immersion confirmed strong corrosion resistance, with impedance values ($|Z|_{0.01}$Hz) above $10^8\ \Omega{\cdot}cm^2$ [32].

The same group also developed photocurable environmentally friendly anticorrosion coatings utilizing a vanillin-derived epoxy resin (DGEVA) reinforced with nano clay and applied to mild steel substrates. EIS measurements indicated a good anticorrosion performance, with the coatings maintaining impedance modulus values above $10^6\ \Omega{\cdot}cm^2$ even after prolonged immersion in a 3.5% NaCl solution (up to 168 h) [33].

These results emphasize the potential of bio-based photocurable composites as sustainable alternatives to traditional coatings for corrosion protection on metal surfaces.

To the best of Authors' knowledge, only one study by Komartin et al. has focused on the development of photocurable oil-lignin composite coatings for corrosion protection. In this work, they prepared three different formulations containing epoxidized linseed oil (ELO), Araldite HY964 as hardener, Araldite DY064 as accelerator and kraft lignin (LnK) in varying concentrations of 5%, 10%, and 15% [10]. However, the curing system that they used combined two stages: first UV curing (15 min at high intensity – 8 W) followed by a lengthy thermal treatment (23 h at 80 °C), greatly increasing energy consumption and making industrial application nearly impossible. Moreover, the tested coating thickness for corrosion protection was about 500 μm, which is too high for real industrial use.

Although less explored, the Authors believe that the cationic UV-curing technology is very promising as a green technology to produce sustainable anticorrosion coatings, and despite increasing interest in sustainable epoxy systems, to the best of the Authors' knowledge, studies addressing the role of unmodified lignin anticorrosion coatings remain limited.

To address this significant gap in the literature, this study demonstrates the potential of physically mixed ESO–unmodified lignin coatings cured by cationic UV-polymerization, focusing on the development of thin films (55 μm) for corrosion protection. Our focus is on lignin's chemical composition, formulation and curing optimization, as well as corrosion resistance. Additionally, a comprehensive evaluation of the thermal, mechanical, and barrier properties of the obtained coatings is provided.

2. Experimental section

2.1. Materials

The epoxidized soybean oil (ESO) was provided by Cargill Bio-industrial and used without further modification as a biobased epoxy monomer. Commercial technical soda lignin Protobind® 1000 (a mixed wheat straw/Sarkanda grass lignin from soda pulping of non-woody biomass) was purchased from Tanovis (Alpnach, Switzerland) and is referred as lignin in this work. Triarylsulfonium hexafluorophosphate salt (TAS-PF6), mixed at 50 wt% in propylene carbonate, was used as photoinitiator (PhI). Photoinitiator and all solvents of analytical grade were obtained from Merck (Merck Life Science S.R.L., Milan, Italy) and used without further purification. Deuterated solvents were purchased from Eurisotop (Saint-Aubin, France).

2.2. Coatings preparation

To realize the coating, ESO was initially heated to 40 °C to get a fully liquid state. Various concentrations of lignin were added, as shown in Table 1. Before mixing, the lignin was dried in an oven at 60 °C for 24 h to remove excess moisture. The ESO and lignin mixture was stirred using an IKA ULTRA-TURRAX® digital disperser to ensure a uniform lignin dispersion. This blend was homogenized at 20,000 rpm for 5 min. Then, TAS-PF6 salt mixture was added as the cationic photoinitiator, in a concentration of 5 phr (per hundred resin, actual phI content = 2.5 phr). The mixture was homogenized for an additional 10 min under stirring condition. To further improve dispersion uniformity, the formulation was sonicated for 15 min.

The mild steel substrates (composition: 0.10 wt% C, 0.60 wt% Mn, 0.20 wt% Ni, 0.15 wt% Cr, and balance Fe) were polished with silicon carbide abrasive paper up to 800 grit to have reproducible surface conditions among different samples, and then cleaned in acetone. Using a spiral bar coater, the formulation containing ESO, photoinitiator, and lignin was applied on steel substrates with an average thickness of about 55 µm. The film underwent crosslinking under a Dymax ECE 5000 Flood lamp for 4 min, exposed to UV light with an intensity (UVA) of 35 mW/cm^2.

2.3. Characterization

2.3.1. Lignin solubility in organic solvents

Lignin solubility in the different solvents was determined by treating 1 g of lignin with 10 mL of the required solvent under stirring at 400 rpm. Each test was carried out overnight at room temperature. The suspension was then filtered, and the residual solvent was evaporated at reduced pressure, and the final residue was dried until a constant weight was achieved prior to quantification [34].

2.3.2. Folin–ciocalteu analysis

The total phenolic content of the lignins was determined via a modified Folin–Ciocalteu (FC) protocol with some adaptation to the sample preparation step, as previously described [35]. Briefly, the samples were dissolved in dimethyl sulfoxide (DMSO) with a final concentration of 2 mg/mL. 5 µL of working solution was mixed with 120 µL of deionized water and 125 µL of FC reagent (Sigma 47,641), stirred with vortex and kept for 6 min at room temperature. Then, after the addition of 1.25 mL of 5% sodium carbonate and mixing, the vial was incubated in a thermoshaker at 40 °C for 30 min. The absorbance was measured in a 1 cm optical path cuvette at 760 nm and 25 °C using a UV–Vis spectrophotometer (Jasco V-560) equipped with a temperature-controlled cuvette holder and a thermostatic water bath (Haake K10, Karlsruhe, Germany). Deionized water was used as the blank sample and vanillin as the reference standard. The calibration curve was constructed with nine different vanillin solutions in DMSO with a concentration in the range 0–500 µg/mL and each FC assay determination was carried out in triplicate.

2.3.3. ^{31}P NMR analysis

To ^{31}P NMR spectroscopic analysis was carried out on a Bruker Instrument AVANCE400 spectrometer (Milano, Italy). Acquisition and data treatment were performed with Bruker TopSpin 3.2 software (Milano, Italy). The spectrum was collected at 29 °C with a 4-s acquisition time, 5-s relaxation delay, and 256 scans. Prior to analysis, lignin sample was dried for 24 h under vacuum and then derivatized according to a previously described procedure [36].

Briefly, lignin (40 mg) was completely dissolved in 300 µL of *N*,*N*-dimethylformamide. Then 200 µL of dry pyridine, 100 µL of solution of internal standard (10 mg of Endo-*N*-hydroxy-5-norbornene-2, 3-dicarboximide (Sigma 226,378) dissolved in 0.5 mL of a mixture of pyridine and $CDCl_3$ 1.6:1 *v/v*), 50 µL of a relaxation agent solution (5.7 mg of chromium (III) acetylacetonate (Sigma 574,082) dissolved in 0.5 mL of a mixture of pyridine and $CDCl_3$ 1.6:1 *v/v*), 100 µL of 2-chloro-4,4,5,5-tetramethyl-1, 3,2-dioxaphospholane (Sigma 447,536), and 200 µL $CDCl_3$ were mixed. The solution was then centrifuged and filtered. All chemical shifts reported were related to the reaction product of the phosphorylating agent with water, which gave a signal at 132.2 ppm.

2.3.4. Viscosity and photo-rheology

Viscosity measurements were carried out using the Anton Paar MCR 702e (Graz, Austria) rheometer with a parallel plate geometry. The setup consisted of two flat plates with a 300 µm gap, and measurements were conducted at a controlled temperature of 25 °C. Viscosity was recorded as a function of shear rate ($\dot{\gamma}$), ranging from 100 s^{-1} to 0.1 s^{-1}. The rheological behavior of the tested formulations was then analyzed using the power law model (two-term model, Eq. 1) and the Sisko model (three-term model, Eq. 2) [7].

$$\eta = K\dot{\gamma}^{n-1} \tag{1}$$

$$\eta = \eta_{\infty} + K\dot{\gamma}^{n-1} \tag{2}$$

where η denotes viscosity, $\dot{\gamma}$ signifies the shear rate, K indicates the consistency index, n refers to the flow behavior index, and η_{∞} represents viscosity at infinite shear rate.

Photo-rheology experiments were conducted using the same instrument, an Anton Paar Modular Compact Rheometer equipped with a parallel plate configuration with a quartz bottom plate to allow UV light transmission. The gap was fixed at 300 µm, and all measurements were performed at 25 °C. Time-sweep tests were conducted in the linear viscoelastic region (LVR) of the formulations, previously determined by an amplitude sweep test, under a constant strain amplitude of 0.5% and an angular frequency of 6 rad/s. UV irradiation was initiated after 30 s using a UV Hamamatsu LC8 lamp (Hamamatsu City, Japan) at an intensity of 32 mW/cm^2, with light exposure from the bottom. The evolution of G′ and G″ was monitored over time to assess the kinetics of crosslinking.

2.3.5. Fourier transform infrared spectroscopy (FTIR)

FTIR spectra were recorded using a Nicolet iS50 Spectrometer in transmission mode. Formulations were applied onto a silicon wafer with an average thickness of 12 µm. Measurements covered a wavenumber range from 500 cm^{-1} to 4000 cm^{-1}. The spectra were collected before and after UV irradiation under the Dymax lamp (100 mW/cm^2). All spectra were acquired in air, with a scanning rate of one scan per 1.2 s and a spectral resolution of 4.0 cm^{-1}. Data were processed using Thermo Scientific OMNIC Spectra Software, with each measurement performed in duplicate for reliability. The epoxy group conversion was assessed by monitoring the decrease in intensity of the absorption peak at 840 cm^{-1}, specific to epoxy functional groups. The epoxy group conversion was calculated using Eq. 1, where A_{pre} and A_{post} represent the peak areas of the epoxy group before and after curing, respectively. The area of the carboxylic group C═O centred at 1800 cm^{-1} was used to normalize [37,38].

$$Conversion\ (\%) = \left(1 - \left(A_{post}\ /A_{pre}\right)\right) \times 100 \tag{3}$$

2.3.6. Dynamic thermal-mechanical analysis (DMTA)

The thermomechanical response of the coatings was measured using dynamic mechanical thermal analysis (DMTA) on an MCR 702e

Table 1
Composition of the photocurable formulations.

Formulation	Epoxy monomer	Lignin [%wt]	TAS-PF_6 (phr)
L0	ESO	0	2.5
L1	ESO	1	2.5
L3	ESO	3	2.5

MultiDrive modular compact rheometer (Anton Paar, Graz, Austria) in tensile mode. The specimens have dimensions of 20 × 5 × 0.3 mm^3 (length × width × thickness). Temperature sweeps were performed from −70 °C to 100 °C at a frequency of 1 Hz and within the linear viscoelastic region (0.1% extensional strain). Both loss modulus (E″) and storage modulus (E′) were recorded, and tan δ values were calculated and plotted as a function of temperature.

2.3.7. Differential scanning calorimetry (DSC)

DSC was used in this study to evaluate the thermal transitions of the ESO–lignin composites in comparison to the pristine ESO sample. Measurements were conducted using a DSC 214 Polyma instrument (NETZSCH-Gerätebau GmbH, Germany) at a heating rate of 10 °C/min, employing 100 μL aluminum crucibles with perforated lids under an Argon atmosphere.

2.3.8. Thermogravimetric analysis (TGA)

TGA was conducted using a Mettler Toledo TGA/SDTA 851e to assess the thermal stability of the films obtained. Samples weighing 10–12 mg were placed in alumina cups and heated at a rate of 10 °C min^{-1} from 25 °C to 800 °C under air flow.

2.3.9. Pencil hardness

The pencil hardness test was conducted according to the ASTM D3363–74 standard [39], beginning with 6H pencils. Each pencil was positioned at a 45° angle and dragged across the surface for at least 6 mm, applying uniform pressure and speed. The surface hardness was identified as the highest pencil that made a scratch no longer than 3 mm within the 6 mm test part, signifying surface damage.

2.3.10. Coating adhesion

Coating adhesion on mild steel substrates (same composition reported above) was tested following ASTM D3359—B standard [40]. A cross-hatch pattern was made with a six-tooth blade at 2 mm spacing. Adhesive tape was pressed onto the grid and removed at 180°. Adhesion was rated by visually estimating undamaged squares after tape removal, as per ASTM procedure.

2.3.11. Solvent rub resistance test

Solvent resistance was tested using the ASTM D5402 [41]solvent rub method. A toluene-soaked cotton cloth was applied to a 100 × 25 mm^2 coated surface with moderate pressure (1000–2000 g). The fabric stayed saturated during testing. Rubbing back and forth, each motion counted as one double rub, and continued until either metal surfaces appeared or 200 rubs were reached.

2.3.12. Contact angle

Contact angle measurements were carried out using an OCA 20 goniometer (Dataphysics Co., Germany), equipped with a high-resolution CCD camera and a 500 μL Hamilton syringe. At room temperature, droplets of testing liquids were deposited on the coating surfaces using the sessile drop method. The system recorded sequential images at a capture rate of 30.02 frames per second. Each contact angle was computed using integrated image analysis software, and the measurements were repeated twice for reproducibility. The surface free energy was determined on the basis of Owens-Wendt-Rabel-Kaelble (WORK) method (Eq. 4):

$$\frac{(1+cos\theta)\cdot\gamma_l}{2\sqrt{\gamma_l^D}} = \sqrt{\gamma_s^p\sqrt{\frac{\gamma_l^p}{\gamma_l^D}}+\sqrt{\gamma_s^D}} \quad (4)$$

The measuring liquids were double-distilled water (γ_l^D = 21.8 mN m^{-1} -Surface tension dispersive component;γ_l^p =*51* mN m^{-1}-Surface tension polar component;γ_l = 72.8 mN m^{-1}-liquid surface tension) and glycerol (γ_l^D = *37* mN m^{-1}-Surface tension dispersive component;γ_l^p =*26.4* mN m^{-1}-Surface tension polar component;γ_l = 63.4 mN m^{-1}-liquid surface tension); θ is the contact angle measured for the tested liquid [42,43].

2.3.13. Inhibition halo test

The antibacterial performance of the samples against MDR *Staphylococcus epidermidis* (ATCC 29213) was evaluated using the Kirby–Bauer disk diffusion method, following the National Committee for Clinical Laboratory Standards NCCLS M2-A9 standard [44]. Circular specimens with a diameter of 8 mm were placed on Mueller–Hinton agar plates evenly inoculated with bacterial solutions (McFarland index 0.5). The plates were then incubated at 35 °C for 48 h. After incubation, the zones of inhibition around each sample were observed. Using Image J software, the Zones of Inhibition (ZOI) produced by different samples were measured to evaluate their antibacterial activity.

2.3.14. Electrochemical characterizations

The corrosion resistance of the coated steel samples was tested using Electrochemical Impedance Spectroscopy (EIS) measurements, acquired with an IVIUnSTAT system, a multichannel electrochemical interface connected to a three-electrode cell. The setup included an Ag/AgCl reference electrode, a Pt wire as the counter electrode, and the coated steel as the working electrode, following standard protocols. Electrochemical impedance was measured over the frequency range from 10^{-2} Hz to 10^4 Hz using a 10-mV sinusoidal signal, with 10 data points recorded per frequency decade. All experiments were carried out in a 3.5 wt% NaCl solution at room temperature to simulate the aggressivity of marine environments. The working electrode area was 0.785 cm^2; all reported impedance data were normalized to a 1-cm^2 surface. Measurements were carried out after 1 h of immersion in the electrolyte and were performed every 24 h for about 14 days, to assess the stability of the coatings as a function of the exposure to the aggressive electrolyte. Impedance spectra were analyzed by means of equivalent electrical circuits (EEC) modeling, using the software IviumSoft 4.1196 to allow a quantitative evaluation of coating protective capability over time. Each coating formulation was tested 3 times to ensure statistical reliability of the results.

2.3.15. Field emission scanning electron microscope (FESEM)

Surface morphology of the coated steel samples was analyzed after corrosion tests using a Zeiss SUPRA 40 Field Emission Scanning Electron Microscope. For high-resolution imaging, samples were sputter-coated with a thin platinum layer (about 12 nm) via a Quorum Q150TS Sputter Coater, operated at 30 mA for 20 s in argon atmosphere. The samples were then mounted on SEM stubs with carbon tape and examined under high vacuum at accelerating voltages ranging from 5 kV to 15 kV.

3. Results and discussion

3.1. Lignin structure evaluation

The lignin exploited in the present work is a high-purity aromatic biopolymer obtained from annual plants. In particular, it is a mixed wheat straw/Sarkanda grass lignin recovered from soda pulping of non-woody biomass whose commercial name is Protobind 1000. This lignin has been fully characterized in terms of molecular mass, solubility in organic solvents, and hydroxyl group content. The value of number-average molecular weight (Mn), weight-average molecular weight (Mw), and dispersity (Đ) were respectively 1390 g/mol, 4660 g/mol, and 3.30, showing a certain degree of hydrolysis of lignin, probably due to the pulping process.

The solubilization studies are a key step in lignin characterization and valorization. In fact, one of the main drawbacks currently hampering effective lignin exploitation is its poor solubility in aqueous systems and in the most commonly used organic solvents. The solubility

of lignin has been tested with water and six organic solvents, namely *n*-butyl acetate (BuOAc), ethyl acetate (EtOAc), 2-butanone (MEK), methanol (MeOH), *tert*-butyl methyl ether (MTBE), and tetrahydrofuran (THF). The resulting extraction yields (as *w*/w percent of solubilized fraction vs. total fraction) are reported in Fig. 1 (with water solubility as the comparison).

This lignin, as expected, was quite insoluble in water, but on the other hand, it was soluble in the selected organic solvents, in particular in MEK, methanol, and THF, with a solubility of around 80% (w/w). This characteristic is important because it offers a significant advantage for the further exploitation of lignin in coatings technology.

The hydroxyl content of lignin was investigated using two different tests. The total phenolic content was determined using a modified Folin Ciocalteu (FC) assay. The classical test is based on the reaction of phenolic hydroxyl groups with a specific redox reagent (FC reagent), leading to the formation of a blue chromophore that is, however, sensitive and unstable in strong bases. Therefore, based on an analytical protocol previously set up [36], DMSO was used as solvent for the samples in order to obtain their complete solubilization in neutral conditions. The phenolic content, expressed as vanillin equivalents (mmol/g of dry lignin), is reported in Table 2 and amounts to 3.06 mmol/g. The total hydroxyl groups quantification has also been investigated using ^{31}P NMR technology (Fig. S1). To perform the hydroxyl attribution of signals, the spectrum was analyzed and integrated from 150 to 147 ppm (signals associated with aliphatic hydroxyl groups), from 145 to 138 ppm (signals associated with aromatic hydroxyl groups), whereas signals centred on 136 ppm accounted for the carboxylic acid residues. The peak integration in these three parts of the spectra led to the quantification of the total hydroxyl groups expressed in mmol of functional group per gram of lignin as reported in Table 2 below.

Lignin showed interesting values of vanillin equivalents (3.06 mmol/g) and aromatic hydroxyl groups (4.67 mmol/g). The proportion of aliphatic -OH and oxidized carboxylic groups appeared to be lower. These results constitute a very important tool for the exploitation of this product in the preparation of lignin-based coatings where the presence of such functionalities has already been proven to act as corrosion inhibitors [45].

Moreover, in our previous work the pyrolysis chromatography/mass spectrometry (Py-GC/MS) was used to precisely evaluate in the lignin structure the: syringyl (S), guaiacyl (G), and *p*-hydroxyphenyl (H) (S:G:H) units distribution which were found to be [46]: (S) 59.3%, (G) 30.9%, and (H) 9.8%. Interestingly, this S-G-H ratio is similar to the one previously reported for organosolv ligning derived from beech (55.4/1.3/43.3) successfully used for the production of anticorrosion coatings [22].

Table 2
Detailed hydroxyl/carboxyl quantification by Folin Ciocalteu analysis and ^{31}P NMR (as mmol of functional group per g of dry lignin).

Sample	Vanillin Equivalents Content (mmol/g)	-OH Aliphatic (mm/g)	-OH Aromatic (mm/g)	-COOH (mmol/g)
Protobind 1000	3.06	3.00	4.67	1.42

3.2. Viscosity analysis

The viscosity of photocurable resins is a key factor in coating applications, as rheological properties influence both processability and performance. As shown in Fig. 2, samples L0 and L1 demonstrated a non-Newtonian-behavior: their viscosity decreased steadily as shear rate increased, leveling off at a second Newtonian plateau at high shear rates. This behavior can be fitted by the Sisko model (Eq. 2), with low flow behavior of $n = 0.04$ and $n = 0.08$, indicating a strong shear-thinning response. This behavior can be explained by the presence of entanglements between the ESO molecules, which break down with increasing shear rate. Conversely, sample L3 exhibited Newtonian behavior throughout the entire shear rate range, maintaining nearly constant viscosity. Its behavior was better represented by the Power Law model (Eq. 1), with a flow index n ≈ 1.0 and an average viscosity of 411 mPa·s. This behavior can be explained considering that the lignin at 3 wt% can effectively act as plasticizer or have an effect as chain disentanglement effect [47]. In fact, lignin molecules are hyper-branched rigid polymers ($M_w < 5000$ g/mol) that cannot form coils like small molecules or linear polymers and therefore can act as lubricant by pushing the ESO chains away from each other, reducing the entanglements and increasing the free volumes of the system [48,49].

The viscosity model parameters for all samples are summarized in Table 3.

Moreover, as can be seen in Fig. 2, a slight enhancement of viscosity in the Newtonian plateau region is observed with the addition of lignin; this behavior can be explained considering the strong intramolecular interaction (hydrogen bonding) between the hydroxyl groups of lignin and the epoxy ring and ester groups of ESO.

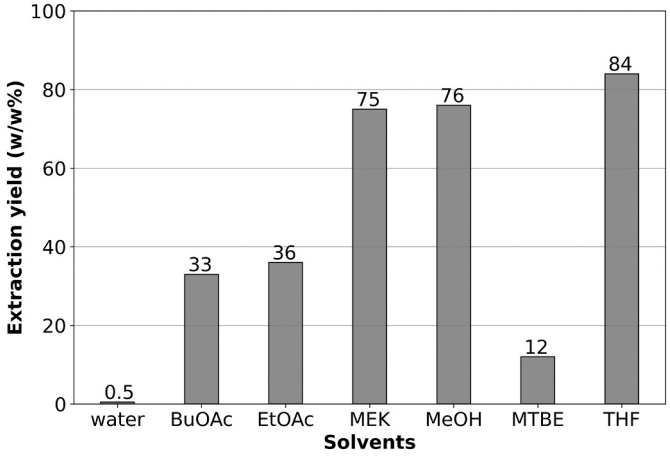

Fig. 1. Extraction yield of lignin Protobind 1000. The data are reported as the percent (*w*/w) of solubilized fraction vs. total fraction in 5 different organic solvents and water.

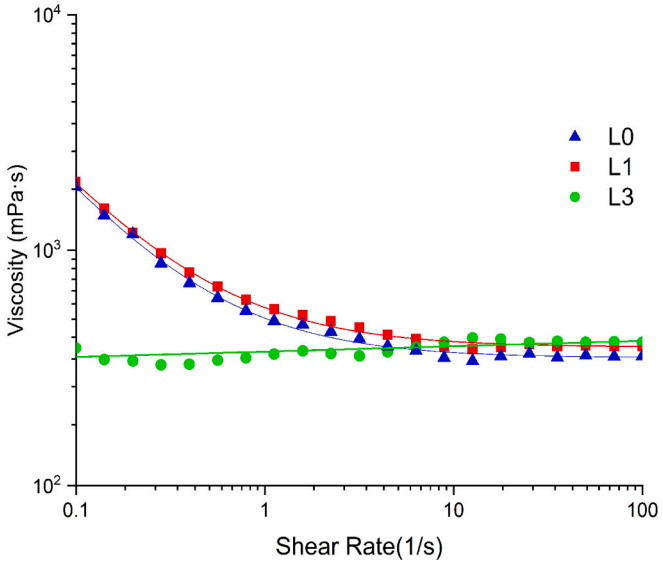

Fig. 2. Viscosity Curves of the 3 formulations before curing. The markers are the experimental points, while the continuous lines represent the model (Sisko model for L0 and L1, Power Law model for L3).

Table 3
Viscosity models parameters.

Sample	Fitting Model	K	n	η_∞ [mPa·s]	η [mPa·s]
L0	Sisko	165	0.04	349	353
L1	Sisko	183	0.08	387	390
L3	Power law	371	1	–	411

Table 4
Crosslinking parameters of ESO formulations.

Sample	L0	L1	L3
Onset Time (s)	40	50	75
Gelation Time (s)	78	109	177
Conversion (%)	64	85	78

3.3. Photo-reactivity

By using real-time photo-rheology, the curing behavior and kinetics were monitored by following the enhancement in the storage modulus (G') caused by the crosslinking reaction [50]. As reported in Fig. 3, when light was turned on, a delay was observed before the actual increase of the storage modulus, which is called 'induction time', and it increases with the lignin content. During the early cure stage, the resin is in a liquid state, and G" (loss modulus) exceeds G'. As polymerization progresses, molecular weight and cross-linking density rise, resulting in an enhancement of both the G' and G" moduli values. During the curing of the thermosets, a G'-G" cross-over is observed, defined as gel point, which indicates the point at which the polymer changes from a viscous liquid into an elastic gel, gaining elastic properties absent in the liquid state, thus marking the first stage of elasticity dominance [51,52]. The gel point of the different formulations is reported in Table 4. As can be observed in Table 4, the gelation and the induction time increase as the lignin content increases, probably due to the partially UV-shielding effect of the aromatic groups of lignin, which slows down the network formation.

Additionally, from the slope of the G' curve, the kinetics of the photopolymerization can be estimated, and it decreases with increasing lignin content. This further confirms the UV-shielding effect of lignin [53].

FTIR measurements were subsequently performed to investigate the chemical structure changes of formulations during the reaction. As shown in Fig. 4, the addition of lignin into the ESO did not cause a significant shift in the peak positions of the ESO FTIR spectrum. However, the absorption peak intensities related to C═C stretching vibrations in aromatic rings region around 1600–1500 cm^{-1} became more prominent with increasing lignin content, especially in the L3 sample. This enhanced intensity reflects the higher aromaticity introduced by lignin [54]. The spectra displayed several significant vibrational bands linked to the functional groups in the ESO-based composite. In particular, absorption peaks at 2926 $cm^{-1}$and 2854 cm^{-1} correspond to the asymmetrical and symmetrical stretching vibrations of methylene

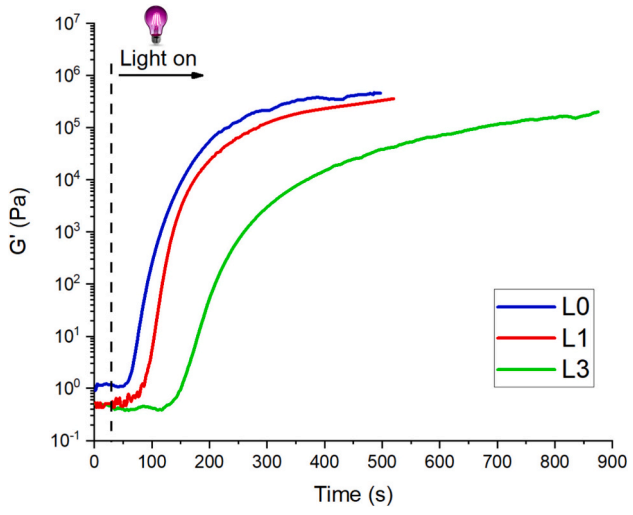

Fig. 3. Photo-rheology curves showing the evolution of the storage modulus (G') over time.

(–CH_2–) groups. A prominent band at 1735 cm^{-1} is linked to the stretching vibration of ester carbonyl (C=O) groups, which is part of the triglyceride structure of ESO [55]. Additional peaks at 1465 cm^{-1} and 1387cm^{-1} were detected, representing the scissoring and rocking modes of C—H bonds in CH_2 and CH_3 groups. The interval between 1162 cm^{-1} and 1116 cm^{-1} is attributed to C—O bending and stretching vibrations, respectively. A particularly notable signal at 840 cm^{-1} is related to the epoxy ring [56].

To further investigate the epoxy group conversion of the composites, FTIR analysis was performed on the formulations before and after the UV-curing process (See Fig. 4). After the UV irradiation, a notable reduction in the 840 cm^{-1} peak was observed, confirming the success of the cationic epoxy group opening reaction. Moreover, two new absorption peaks can be observed: one at 1090 cm^{-1} associated with ether linkages, and another broad band near 3465 cm^{-1}, corresponding to O—H stretching vibrations, which indicates the formation of hydroxyl groups as a consequence of the ring-opening process, thus further confirming the success of the epoxy group reaction [57].

As reported in Table 4, the formulations containing lignin showed the higher epoxy conversion, up to 85% (L1) with respect to pristine ESO formulation. This can be explained by either the ability of lignin to act as a photosensitizer [45,46] or by the lignin's phenolic and hydroxyl functional groups, which can engage in secondary polymerization reactions, thus boosting the efficiency of the photopolymerization reaction [47]. In particular, this secondary reaction pathway, known as the Activated Monomer Mechanism (AMM), as described by Penczek and Kubisa, occurs during the cationic polymerization of epoxides in the presence of hydroxyl (OH) groups [27,58,59].

In this process, the growing ionic chain-end is subject to nucleophilic attack by the OH group, leading to the formation of a protonated ether. The subsequent deprotonation of this species by the epoxy monomer results in the termination of the growing chain and facilitates the transfer of protons to new monomers. This results in the partial chemical incorporation of lignin into the network, leading to the formation of more flexible ether structures and higher epoxy group conversion (Scheme S1).

Finally, L3 showed lower conversion with respect to L1, further confirming lignin's UV shielding effect as its aromatic groups can partially absorb UV light, thereby limiting the UV-light penetration [48].

3.4. Thermal properties

The thermal characteristics of the ESO–lignin samples were evaluated by DMTA, DSC and TGA.

Both DSC (Fig. S2) and DMTA (Fig. S3) results are reported in Table 5. As can be observed in the table, with high lignin content (L3), the glass transition temperature increases, indicating the formation of a more rigid polymer network. This suggests that lignin particles can effectively act as a reinforcing agent for the ESO matrix, restricting the polymer chain mobility. This reinforcement is further evidenced in the DMTA spectra (Fig. S3), in which it is possible to observe that the addition of 3 wt% lignin leads to an enhancement of the storage modulus in both the elastic and plastic plateau regions [49].

This enhancement, however, was not observed at the lower concentration. The L1 composite showed negligible reinforcement, with its glass transition and rubbery plateau modulus remaining similar to the

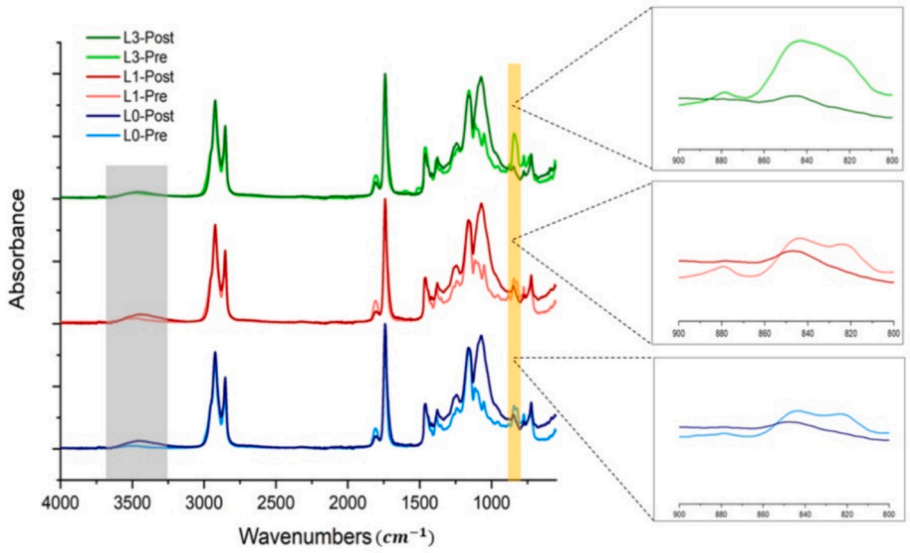

Fig. 4. FTIR spectra before and after UV curing (indicated as -Pre and -Post, respectively) of ESO and ESO composites.

Table 5
Thermal properties of the crosslinked ESO composite films.

Sample	Tg_{DSC} (°C)	Tg_{DMTA} (°C)	E'_{elastc} (MPa)	E'_{rub} (MPa)	$T_{(5\%)}$ (°C)	T_{Peak} (°C)	Char Residue (%)
L0	−22	−11	1148.6	7.1	282	375/558	0.08
L1	−23	−12	350.4	7.5	273	377/565	0.15
L3	−20	4	2579.7	18.3	277	379/562	0.22
Lignin	–	–	–	–	201	257/473	2.46

control (L0). Notably, a slight reduction in the glassy-state storage modulus was observed in L1 composite.

This result is consistent with the AMM secondary reaction mechanism discussed above, where the formation of flexible ether groups within the network introduces localized plasticization, effectively dissipating mechanical energy and reducing the load-transfer capability expected from the dispersed lignin.

According to the TGA and DTG results (see Fig. S4), lignin exhibits two-step decomposition. The first minor degradation occurs at around 257 °C, due to the release of moisture and low-molecular-weight volatiles, while the main degradation stage appears at 473 °C, corresponding to the decomposition of the aromatic backbone [60].

A similar two-step pattern is observed in the DTG curves of the ESO-based coatings containing different amounts of lignin, and as shown by the data in Table 5, all samples display very similar thermal stability, indicating that adding lignin to the ESO matrix does not noticeably change the overall thermal behavior of the system. The onset of degradation, defined as the temperature at 5 wt% mass loss (T_5%), is 282 °C for the neat ESO coating and decreases slightly upon lignin incorporation, indicating a modest reduction in early-stage thermal stability. Furthermore, a slight enhancement of the char residue with the addition of lignin can also be noticed, as expected from the higher number of aromatic groups present inside the lignin [61].

3.5. Surface properties

The physical-chemical properties of the UV-cured film improved with lignin addition in comparison with the pristine formulation (see Table 6). In the pencil hardness test, the hardness improved from B (for L0 sample) to H in L1 and 2H in L3 samples, demonstrating enhanced surface rigidity attributed to the incorporation of lignin.

The same trend was observed in the cross-cut tape test, in which L3 samples demonstrated good adhesion, with no visible detachment or edge lifting, earning a 5B rating. The adhesion of the coating to the metal surface is a key factor in its corrosion resistance. Without proper adhesion, the coating may detach, leading to corrosion over time. In organic coatings for metal substrates, the adhesion can be of two types: mechanical and chemical. Mechanical adhesion occurs when coatings penetrate surface metal pits and create mechanical bonds. This type of adhesion can be enhanced by increasing the roughness of the substrate. Instead, chemical adhesion involves the formation of interatomic bonds at the interface between the substrate and the coatings. There can be identified different types of bonds: primary (covalent or ionic), secondary (dispersion, dipole, van der Waals), and hydrogen bonds; however, organic coatings mainly rely on hydrogen or secondary bonds, especially since metal surfaces typically have oxide layers that promote hydrogen bonding with polar binder groups [45,62]. Therefore, the coating's bond strength is highly dependent on the hydroxyl group content of the formulation, which explains why the addition of lignin

Table 6
Surface properties of the crosslinked coatings.

Sample	Coating Hardness	Coating Adhesion	Solvent Resistance (double rubs)	Contact Angle		Surface Free Energy (mN/m)
				Water (°)	Glycerol (°)	
L0	B	1B	11	78 ± 2	87 ± 4	33
L1	H	3B	25	75 ± 1	79 ± 3	31
L3	2H	5B	23	85 ± 3	79 ± 2	23

with a high -OH group content (as demonstrated before) enhances the coating's adhesion.

Subsequently, the coating's solvent resistance was evaluated using an industrially common test: the double-rub test with toluene. L0 samples withstood 11 double rubs before degrading, while L1 and L3 samples withstood 25 and 23 double rubs, respectively. These results, although slightly lower than those reported in the literature [63], indicating that lignin addition increased the solvent resistance of the coatings.

In summary, lignin addition improved the hardness, adhesion, and chemical resistance of the UV-cured coatings compared to the original formulation. Those characterizations provide valuable insight into the overall behavior of the developed materials and support their future application in the coating industry. Moreover, as discussed in the next section, they correlate with the coatings' anticorrosion properties.

The results from the static wettability tests in Table 6 demonstrate that incorporating 3 wt% lignin into ESO-based coatings results in a higher contact angle with water, leading to slight improvement of the hydrophobicity of the film [64]. Moreover, the addition of lignin lowers the surface tension of the ESO coatings, which explains why water (a liquid with high surface tension) shows poor wetting capacity. This can be attributed to the high aromatic-hydrophobic content in lignin's backbone.

In order to test the antibacterial performance of the coatings, the inhibition halo test was performed using the Kirby-Bauer disk diffusion method, and the outcomes are presented as inhibition zone diameters in Fig. 5. The sample containing only ESO showed the smallest inhibition zone among the three formulations, but the values were comparable to those previously reported in the literature for a thermally cured ESO sample against *Staphylococcus aureus* and *Escherichia coli* [65]. With lignin addition, the inhibition zone expanded, indicating improved antibacterial activity. This enhancement is related to lignin's natural antibacterial properties, as its phenolic groups are known to damage bacterial cell membranes, causing rupture, leakage of cell contents, and bacterial death [66].

3.6. Anticorrosion performance

The corrosion protection effectiveness of the coatings in a saline environment was investigated using EIS measurements. As an initial comparison, the barrier properties after 24 h of immersion in the electrolyte were assessed considering the impedance modulus measured at 0.01 Hz. Indeed, this is generally considered a good parameter to compare the behavior of different materials because it is inversely proportional to the corrosion rate. As can be seen from Fig. 6, the highest impedance modulus was measured for the L3 samples, which reached about $3{\cdot}10^8$ Ω·cm^2, while L0 samples did not show an effective protective behavior for the steel substrate, as the impedance modulus was

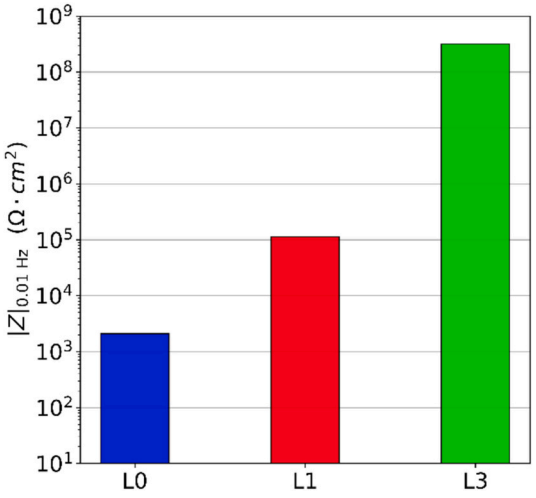

Fig. 6. Impedance modulus (|Z|) measured at 0.01 Hz, acquired after 24 h of immersion in the 3.5 wt% NaCl electrolyte.

below 10^4 Ω·cm^2 already after 24 h of immersion in the electrolyte (see Fig. S5 in Supplementary Materials for the complete impedance spectrum of L0 sample). As a rule of thumb, an organic coating is considered non-protective if the impedance modulus falls below 10^5 Ω·cm^2 [67]. L1 samples showed an intermediate behavior, with a measured impedance modulus of about 10^5 Ω·cm^2.

It is worth noting that, in order to obtain acceptable barrier properties for the L0 samples, the thickness had to be increased up to 100 μm (experimental data not reported in the present manuscript). Considering that such a high thickness would not be sustainable from an economic point of view and would constitute a huge consumption of material in future applications, this formulation was not further investigated, and the following corrosion tests focused only on L1 and L3 samples.

The impedance spectra acquired on L1 and L3 samples during the 2-week immersion in 3.5 wt% NaCl electrolyte are reported in Fig. 7 as Bode diagrams. As can be seen, L3 samples show the best protective behavior since the beginning of the test, characterized by a very high impedance modulus (above $2{\cdot}10^8$ Ω·cm^2 at low frequencies) and phase values that remain close to −90° for a wide frequency range. The acquired spectra remain almost unchanged until the end of the test (after 316 h), demonstrating that, despite the water absorption during the immersion period, the coating is able to preserve its barrier properties and to protect the steel substrate. On the other hand, L1 samples exhibit a less protective behavior at the beginning of the test, highlighted by the lower impedance modulus and by the phase values, which remain close

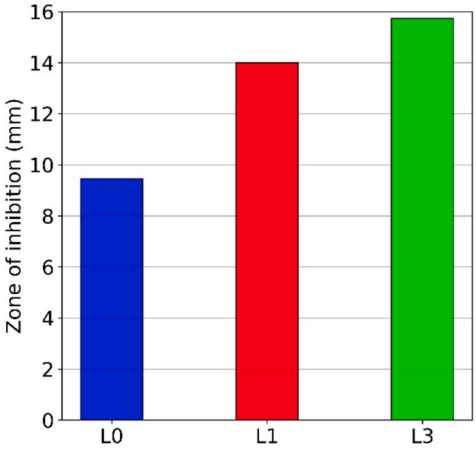

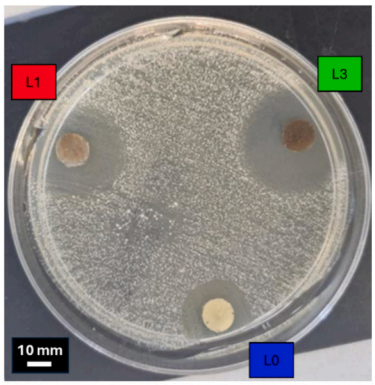

Fig. 5. Inhibition zone diameter for ESO and composite samples.

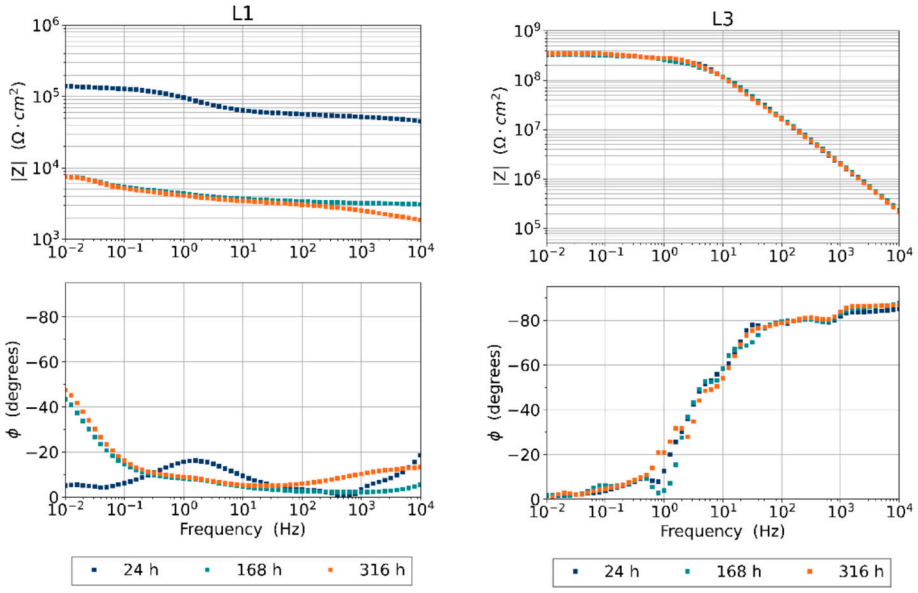

Fig. 7. Impedance spectra presented as Bode diagrams acquired for the L1 and L3 coatings as a function of the immersion time in the 3.5% NaCl solution.

to −20° (i.e. close to resistive behavior) for the whole investigated frequency range. As the immersion time increases, the electrolyte is able to diffuse through the coating, leading to a significant decrease in the impedance modulus, of more than one order of magnitude. Thus, the protective capability decreases significantly by the end of the test.

The different performance of the coatings was also highlighted by the morphological characterization of the samples' surface at the end of the test. As can be seen from Fig. 8, L1 samples show a higher surface roughness, induced by the water absorption. At the same time, in many areas of the sample surface, it was possible to find the presence of pores, which constitute a preferential path for electrolyte diffusion toward the steel substrate (yellow arrow in Fig. 8a). On the other hand, the superficial morphology of the L3 samples was more homogeneous, and no significant defects could be found (see Fig. 8b). As can be seen from Fig. S6, both formulations exhibit a smooth surface and limited roughness before immersion in the electrolyte.

Thus, these results clearly demonstrate the positive effect of lignin on improving the barrier properties of the coatings. This is correlated to the chemical-physical properties that were previously investigated. Indeed, the improved barrier properties in L3 samples are associated with a higher material hardness and hydrophobicity, which hinder the diffusion of the water molecules inside the coating. Moreover, the better adhesion to the metal substrate further improves the corrosion protection effectiveness, because it prevents the coating detachment even when, after many days of immersion, the water molecules have diffused inside the organic material. It is worth noticing also that previous studies have demonstrated the effect of lignin as a corrosion inhibitor [19,45]. So the role of this molecule as an antioxidant (thanks to the ability of polyphenols to neutralize free radicals and reactive oxygen species) can further explain the positive effect on the corrosion resistance of the developed coatings.

In order to provide a quantitative description of the electrochemical system, impedance spectra acquired on L3 samples were modeled using Equivalent Electrical Circuits (EEC). Indeed, this allows a deeper interpretation of the electrochemical behavior of the samples and a better understanding of the transport phenomena occurring during the test. The spectra were modeled using a circuit with a single time constant (see Fig. 9), i.e. composed of: R_s to represent the solution resistance, and the parallel of R_{coat} and CPE_{coat} to model the coating resistance and capacitance, respectively. The coating capacitance was modeled using a

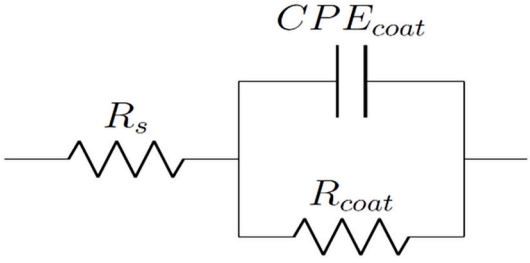

Fig. 9. Equivalent electrical circuit used to model the EIS spectra acquired on L3 samples.

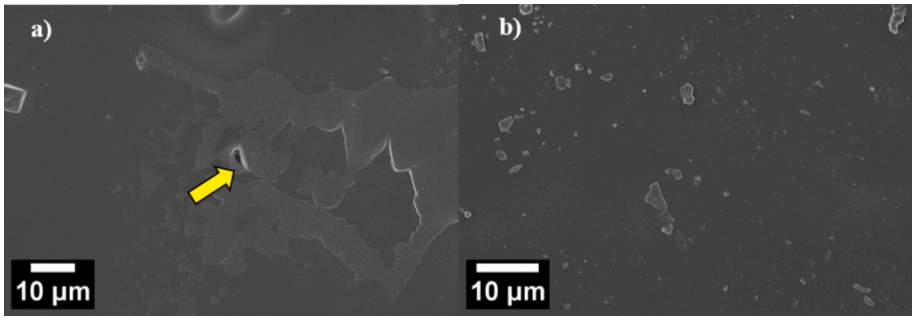

Fig. 8. SEM images showing the morphology of a) L1 and b) L3 samples at the end of the corrosion tests.

Constant Phase Element (CPE), which is characterized by the following frequency response:

$$Z_{CPE} = 1/Q(j\omega)^n \quad 5$$

where Q is the pseudo-capacitance (units of $\Omega^{-1}s^n$), j is $\sqrt{-1}$, $\omega = 2\pi f$ (f is the frequency), and n is a dimensionless parameter ($0 < n \leq 1$) expressing the deviation from ideality ($n = 1$ for an ideal capacitor). The use of a CPE instead of an ideal capacitor allows for the consideration of time constant dispersion, which can arise from surface heterogeneity or non-uniform thickness of the coating.

The values of the components computed at the beginning and at the end of the test (i.e., after 24 and 316 h of immersion, respectively) are reported in Table 7. As can be seen, the value of Rcoat remains almost constant, as well as CPEcoat. This further confirms that the coating is not significantly affected by the permanence in contact with the electrolyte and thus its resistance is almost unaltered. The small variation of the CPE value may be attributed to water absorption, but it does not significantly affect this parameter. Looking at the value for n, this is close to unity, indicating a behavior similar to an ideal capacitor.

4. Conclusion

This study investigated the effect of lignin addition on the chemical-physical properties of biobased organic coatings prepared from ESO. After fully characterizing the biobased filler, three different photocurable formulations were prepared and investigated. As demonstrated, all formulations showed rapid reactivity upon UV exposure and high epoxy-group conversions (above 75%) in all the samples containing lignin. Moreover, the lignin addition improves surface hardness, adhesion to the steel substrate, and increases the hydrophobicity of the material. Furthermore, the addition of lignin enhances the coating's antibacterial properties, as demonstrated by inhibition halo tests against MDR *Staphylococcus epidermidis*.

These characteristics enhance the barrier properties of the coatings, which were tested in a harsh saline environment, a 3.5 wt% NaCl solution. The corrosion tests demonstrated the good protection effectiveness of the samples containing 3 wt% of lignin for up to 2 weeks of immersion in the aggressive electrolyte. Indeed, these very promising results demonstrate the feasibility of developing sustainable UV-curable organic coatings from unmodified renewable sources and pave the way for the use of sustainable materials in coatings for corrosion protection. These results are an important step toward developing a new generation of high-performance, environmentally friendly protective coatings, offering a promising alternative to petrochemical-based systems and contributing to a more sustainable industrial future.

Further research will focus on optimizing lignin formulations to enhance long-term durability under extended environmental exposure and on exploring the scalability and commercial viability of these sustainable coatings. Additionally, life-cycle analysis should be conducted to validate the environmental benefits of using lignin-ESO coatings compared to conventional alternatives.

CRediT authorship contribution statement

Saba Moradi Boldaji: Writing – original draft, Investigation. **Leonardo Iannucci:** Writing – review & editing, Visualization, Supervision, Data curation, Conceptualization. **Sabrina Grassini:** Writing – review & editing, Supervision, Funding acquisition. **Luca Carlomaria Pariani:** Investigation. **Letizia Anna Maria Rossato:** Writing – original draft, Investigation. **Paola D'Arrigo:** Writing – review & editing, Supervision, Funding acquisition. **Camilla Noè:** Writing – review & editing, Visualization, Supervision, Methodology, Data curation, Conceptualization. **Massimo Messori:** Writing – review & editing, Supervision, Funding acquisition.

Table 7
EEC parameters computed from the EIS spectra acquired on L3. See Fig. 9 for the meaning of the electrical parameters.

		24 h	316 h
	R_s [Ohm·cm^2]	10	10
	R_{coat} [Ohm·cm^2]	$3.15 \cdot 10^8$	$3.27 \cdot 10^8$
CPE_{coat}	Q_{coat} [s^n/Ohm·cm^2]	$2.64 \cdot 10^{-10}$	$2.38 \cdot 10^{-10}$
	n_{coat}	0.89	0.88

Declaration of competing interest

The authors declare no conflict of interest.

Acknowledgments

P.D. acknowledges the European Union—Next Generation EU, Mission 4, Component 1, through MUR (Ministero dell'Università e della Ricerca), PRIN 2022, under the project "Biotechnological synthesis of valuable Lipids and fatty acid derivatives from Agro-food industrial Residues" (BioLAR), and CUP B53D23015020006, grant number 20223E9C8S.

Appendix A. Supplementary data

Supplementary data to this article can be found online at https://doi.org/10.1016/j.porgcoat.2026.110024.

Data availability

Data will be made available on request.

References

[1] M. Iannuzzi, G.S. Frankel, The carbon footprint of steel corrosion, Npj Mater. Degrad. 6 (2022) 101.
[2] D. Wang, J. Zhao, P. Claesson, F. Zhang, J. Pan, Y. Shi, Green synergy: Eco-friendly, high-performance anti-corrosion and wear-resistant coatings utilizing organosolv lignin and polydimethylsiloxane, Prog. Org. Coat. 190 (2024) 108365, https://doi.org/10.1016/J.PORGCOAT.2024.108365.
[3] A.M.M. Soliman, K.I. Aly, M.G. Mohamed, A.A. Amer, M.R. Belal, M. Abdel-Hakim, Synthesis, characterization and protective efficiency of novel polybenzoxazine precursor as an anticorrosive coating for mild steel, Sci. Rep. 13 (2023) 5581, https://doi.org/10.1038/s41598-023-30364-x.
[4] M.M. Sayed, S.M. Ahmed, M. Abdel-Hakim, E.-R. Kenawy, K.I. Aly, Design and thermal imidization of new 1,3-thiazine-based polyimides and copolyimides for high-performance corrosion inhibition, Sci. Rep. 15 (2025) 37354, https://doi.org/10.1038/s41598-025-22235-4.
[5] K.I. Aly, J. Sun, D. Kuckling, O. Younis, Polyester resins based on soybean oil: synthesis and characterization, J. Polym. Res. 27 (2020) 286.
[6] M.M. Sayed, A.E.M. Salama, M. Abdel-Hakim, K.I. Aly, Enhancing corrosion protection and luminescence in bio-based polyurethanes with fluorescent azine segments, Prog. Org. Coat. 200 (2025) 109051, https://doi.org/10.1016/j.porgcoat.2024.109051.
[7] C. Noè, L. Iannucci, S. Malburet, A. Graillot, M. Sangermano, S. Grassini, New UV-curable anticorrosion coatings from vegetable oils, Macromol. Mater. Eng. 306 (2021) 2100029.
[8] M. Shahbandeh, Soybean Oil Production Volume Worldwide. https://www.statista.com/statistics/620477/soybean-oil-production-volume-worldwide/, 2025. (Accessed 14 March 2025).
[9] S. Ammar, A.W.M. Iling, K. Ramesh, S. Ramesh, Development of fully organic coating system modified with epoxidized soybean oil with superior corrosion protection performance, Prog. Org. Coat. 140 (2020) 105523, https://doi.org/10.1016/j.porgcoat.2019.105523.
[10] R.S. Komartin, B. Balanuca, M.I. Necolau, A. Cojocaru, R. Stan, Composite materials from renewable resources as sustainable corrosion protection coatings, Polymers (Basel). 13 (2021) 3792.
[11] R. Teijido, L. Ruiz-Rubio, S. Lanceros-Méndez, Q. Zhang, J.L. Vilas-Vilela, Sustainable bio-based epoxy resins with tunable thermal and mechanic properties and superior anti-corrosion performance, Polymers (Basel). 15 (2023) 4180.
[12] S. Ma, Y. Jiang, X. Liu, L. Fan, Bio-based tetrafunctional crosslink agent from gallic acid and its enhanced soybean oil-based UV-cured coatings with high performance, RSC Adv. 4 (2014) 23036, https://doi.org/10.1039/c4ra01311e.
[13] Q. Ma, X. Liu, R. Zhang, J. Zhu, Y. Jiang, Synthesis and properties of full bio-based thermosetting resins from rosin acid and soybean oil: the role of rosin acid derivatives, Green Chem. 15 (2013) 1300–1310.

[14] N.R. Jang, H. Kim, C.T. Hou, B.S. Kim, Novel biobased photo-crosslinked polymer networks prepared from vegetable oil and 2, 5-furan diacrylate, Polym. Adv. Technol. 24 (2013) 814–818.
[15] A. Barkane, E. Kampe, O. Platnieks, S. Gaidukovs, Cellulose nanocrystals vs. cellulose nanofibers: A comparative study of reinforcing effects in uv-cured vegetable oil nanocomposites, Nanomaterials 11 (2021) 1791.
[16] Z. Liu, S.Z. Erhan, D.E. Akin, F.E. Barton, "Green" composites from renewable resources: preparation of epoxidized soybean oil and flax fiber composites, J. Agric. Food Chem. 54 (2006) 2134–2137.
[17] S. Zhou, K. Huang, X. Xu, B. Wang, W. Zhang, Y. Su, K. Hu, C. Zhang, J. Zhu, G. Weng, S. Ma, Rigid-and-Flexible, Degradable, Fully Biobased Thermosets from Lignin and Soybean Oil: Synthesis and Properties, ACS Sustain. Chem. Eng. 11 (2023) 3466–3473, https://doi.org/10.1021/acssuschemeng.2c06990.
[18] M. Wu, B. Cui, H. Liu, Z. Wang, A lignin/castor oil-based polyamide autonomous self-healing composite materials, Int. J. Biol. Macromol. 305 (2025) 141159, https://doi.org/10.1016/J.IJBIOMAC.2025.141159.
[19] D. Wang, P. Claesson, F. Zhang, J. Pan, R. An, Y. Shi, Recent findings on lignin-based wear and corrosion resistance coatings, Corrosion Rev. 43 (2) (2024) 157–174, https://doi.org/10.1515/corrrev-2024-0087.
[20] Y. Zhang, L. Wang, R. Zhao, H. Yue, H. Liu, B. Li, F. Xie, X. Tian, W. Shang, J. Jiang, Y. Wen, Extraction of lignin from lignocellulosic biomass (bagasse) as a green corrosion inhibitor and its potential application of composite metal framework organics in the field of metal corrosion protection, Int. J. Biol. Macromol. 293 (2025) 139271, https://doi.org/10.1016/j.ijbiomac.2024.139271.
[21] S. Akachar, A. AitAghzzaf, Y. Zarki, R. Idouhli, L. Azaryouh, M. El Achaby, K. Draoui, Novel sustainable corrosion inhibitors for enhancing carbon steel corrosion resistance based on clay and lignin biopolymer extracted from raw Alfa fibers, J. Mater. Sci. 59 (2024) 17927–17944.
[22] A. Dastpak, K. Yliniemi, M.C. de Oliveira Monteiro, S. Höhn, S. Virtanen, M. Lundström, B.P. Wilson, From waste to valuable resource: lignin as a sustainable anti-corrosion coating, Coatings 8 (2018) 454.
[23] X. Lai, J. Hu, J. Qu, A mussel-inspired lignin micro-nanospheres/epoxy composite coating with superhydrophobicity, ultraviolet resistance, and photothermal conversion performance for excellent corrosion control, Prog. Org. Coat. 200 (2025) 109049.
[24] J. Wang, F. Seidi, X. Shi, C. Li, Y. Huang, H. Xiao, Lignin self-healing coatings based on thermo-reversible Diels-Alder reaction for anticorrosion applications, Prog. Org. Coat. 191 (2024) 108428, https://doi.org/10.1016/J.PORGCOAT.2024.108428.
[25] O.B.F. Diógenes, D.R. de Oliveira, L.R.R. da Silva, B.G. Linhares, S.E. Mazzetto, D. Lomonaco, W.S. Araujo, Acetylated lignin as a biocomponent for epoxy coating—Anticorrosive performance analysis by accelerated corrosion tests, Surf. Coat. Technol. 474 (2023) 130116.
[26] W.D. Wan Rosli, R.N. Kumar, S. Mek Zah, M.M. Hilmi, UV radiation curing of epoxidized palm oil–cycloaliphatic diepoxide system induced by cationic photoinitiators for surface coatings, Eur. Polym. J. 39 (2003) 593–600, https://doi.org/10.1016/S0014-3057(02)00241-0.
[27] C. Noè, S. Malburet, A. Bouvet-Marchand, A. Graillot, C. Loubat, M. Sangermano, Cationic photopolymerization of bio-renewable epoxidized monomers, Prog. Org. Coat. 133 (2019) 131–138.
[28] F. Deflorian, M. Fedel, 20 - UV-curable organic polymer coatings for corrosion protection of steel, in: A.S.H. Makhlouf (Ed.), Handbook of Smart Coatings for Materials Protection, Ed., Woodhead Publishing, 2014, pp. 530–559, https://doi.org/10.1533/9780857096883.3.530.
[29] S.G. Tan, W.S. Chow, Curing Characteristics and Thermal Properties of Epoxidized Soybean Oil Based Thermosetting Resin, Journal of Oil & Fat Industries 88 (2010) 915–923, https://doi.org/10.1007/s11746-010-1748-x.
[30] H. Li, L. Pei, Y. Liu, B. Liang, Y. Sun, J. Deng, B. Du, S. Zhang, Y. Zhu, H. Wang, A novel UV-curable composite coating with superior anti-corrosion and mechanical properties, Prog. Org. Coat. 196 (2024) 108758, https://doi.org/10.1016/j.porgcoat.2024.108758.
[31] H. Wu, X. Han, W. Zhao, Q. Zhang, A. Zhao, J. Xia, Mechanical and electrochemical properties of UV-curable nanocellulose/urushiol epoxy acrylate anti-corrosive composite coatings, Ind. Crop. Prod. 181 (2022) 114805, https://doi.org/10.1016/j.indcrop.2022.114805.
[32] C. Noè, L. Iannucci, S. Malburet, A. Graillot, M. Sangermano, S. Grassini, New UV-curable anticorrosion coatings from vegetable oils, Macromol. Mater. Eng. 306 (2021) 2100029.
[33] C. Noè, L. Iannucci, S. Malburet, A. Graillot, S. Grassini, Vanillin-Based Photocurable Anticorrosion Coatings Reinforced with Nanoclays, Macromol. Mater. Eng. 309 (2024) 2400155.
[34] C. Allegretti, E. Bellinetto, P. D'Arrigo, G. Griffini, S. Marzorati, L.A.M. Rossato, E. Ruffini, L. Schiavi, S. Serra, A. Strini, Towards a complete exploitation of brewers' spent grain from a circular economy perspective, Fermentation 8 (2022) 151.
[35] L.C. Pariani, F. Castiglione, G. Griffini, L.A.M. Rossato, E. Ruffini, A. Strini, D. Tessaro, S. Turri, S. Serra, P. D'Arrigo, Synergistic DES–Microwave Fractionation of Agri-Food Biomasses in a Zero-Waste Perspective, Molecules 30 (2025) 3588.
[36] C. Allegretti, O. Boumezgane, L. Rossato, A. Strini, J. Troquet, S. Turri, G. Griffini, P. D'Arrigo, Tuning lignin characteristics by fractionation: A versatile approach based on solvent extraction and membrane-assisted ultrafiltration, Molecules 25 (2020) 2893.
[37] S. Malburet, C. Di Mauro, C. Noe, A. Mija, M. Sangermano, A. Graillot, Sustainable access to fully biobased epoxidized vegetable oil thermoset materials prepared by thermal or UV-cationic processes, RSC Adv. 10 (2020) 41954–41966.
[38] C. Noè, S. Malburet, A. Bouvet-Marchand, A. Graillot, C. Loubat, M. Sangermano, Cationic photopolymerization of bio-renewable epoxidized monomers, Prog. Org. Coat. 133 (2019) 131–138, https://doi.org/10.1016/j.porgcoat.2019.03.054.
[39] Test Method for Film Hardness by Pencil Test, 2022, https://doi.org/10.1520/D3363-22.
[40] Test Methods for Rating Adhesion by Tape Test, 2023, https://doi.org/10.1520/D3359-23.
[41] Practice for Assessing the Solvent Resistance of Organic Coatings Using Solvent Rubs, 2024, https://doi.org/10.1520/D5402-19R24.
[42] B. Jańczuk, E. Chibowski, Interpretation of contact angle in solid-hydrocarbon-water system, J. Colloid Interface Sci. 95 (1983) 268–270, https://doi.org/10.1016/0021-9797(83)90096-6.
[43] E. Rynkowska, K. Fatyeyeva, S. Marais, J. Kujawa, W. Kujawski, Chemically and thermally crosslinked PVA-based membranes: effect on swelling and transport behavior, Polymers (Basel). 11 (2019) 1799.
[44] N.C. for C.L.S. (United States), Performance standards for antimicrobial disk susceptibility tests, National Committee for Clinical Laboratory Standards, 2003.
[45] S. Amini, X. Erdocia, J. Labidi, Á.G. Fernández, Lignin based ecological coatings for improved anti-corrosion resistance, Prog. Org. Coat. 200 (2025) 109044, https://doi.org/10.1016/j.porgcoat.2024.109044.
[46] C. Allegretti, S. Fontanay, K. Rischka, A. Strini, J. Troquet, S. Turri, G. Griffini, P. D'Arrigo, Two-step fractionation of a model technical lignin by combined organic solvent extraction and membrane ultrafiltration, ACS Omega 4 (2019) 4615–4626.
[47] E. Selver, A.D. Selver, A. Saifullah, Z. Zhang, H.N. Dhakal, Thermal, Rheological, and Moisture Absorption Behaviours of Polyvinyl Alcohol (PVA)/Lignin Composites, Polymers (Basel). 17 (2025) 2918.
[48] H.C. Liu, C.-C. Tuan, A.A.B. Davijani, P.-H. Wang, H. Chang, C.-P. Wong, S. Kumar, Rheological behavior of polyacrylonitrile and polyacrylonitrile/lignin blends, Polymer (Guildf). 111 (2017) 177–182.
[49] L.T. Possari, R.E.S. Bretas, T.R. Rigolin, S.H.P. Bettini, Dualistic effect of Kraft lignin on the viscoelastic behavior of biodegradable biobased PBSA, Mater. Today Commun. 29 (2021) 102847.
[50] A. Barkane, O. Platnieks, M. Jurinovs, S. Kasetaite, J. Ostrauskaite, S. Gaidukovs, Y. Habibi, Uv-light curing of 3d printing inks from vegetable oils for stereolithography, Polymers (Basel). 13 (2021) 1195.
[51] E. Gazo Hanna, K. Younes, S. Amine, R. Roufayel, Exploring gel-point identification in epoxy resin using rheology and unsupervised learning, Gels 9 (2023) 828.
[52] M.R. Martínez-Miranda, V. García-Martínez, M.R. Gude, Gel point determination of a thermoset prepreg by means of rheology, Polym. Test. 78 (2019) 105950, https://doi.org/10.1016/J.POLYMERTESTING.2019.105950.
[53] G. Arias-Ferreiro, A. Lasagabáster-Latorre, A. Ares-Pernas, P. Ligero, S.M. García-Garabal, M.S. Dopico-García, M.-J. Abad, Lignin as a high-value bioaditive in 3D-DLP printable acrylic resins and polyaniline conductive composite, Polymers (Basel). 14 (2022) 4164.
[54] A. Rahmani, A. Abdulkhani, A. Ashori, J. Hosseinzadeh, Development of high-performance biocomposites through lignin modification and fiber reinforcement, Sci. Rep. 14 (2024) 28932.
[55] S. Dalle Vacche, L.H. Esposito, D. Bugnotti, E. Callone, S.F. Orsini, M. D'Arienzo, L. Cipolla, S. Petroni, A. Vitale, R. Bongiovanni, Modification of Epoxidized Soybean Oil for the Preparation of Amorphous, Nonretrogradable, and Hydrophobic Starch Films, Polysaccharides 6 (2025) 40.
[56] M. Qi, Y.-J. Xu, W.-H. Rao, X. Luo, L. Chen, Y.-Z. Wang, Epoxidized soybean oil cured with tannic acid for fully bio-based epoxy resin, RSC Adv. 8 (2018) 26948–26958.
[57] H. Yang, J. Irudayaraj, Characterization of semisolid fats and edible oils by Fourier transform infrared photoacoustic spectroscopy, J. Am. Oil Chem. Soc. 77 (2000) 291–295.
[58] S. Penczek, M. Cypryk, A. Duda, P. Kubisa, S. Słomkowski, Living ring-opening polymerizations of heterocyclic monomers, Prog. Polym. Sci. 32 (2007) 247–282, https://doi.org/10.1016/j.progpolymsci.2007.01.002.
[59] P. Kubisa, Hyperbranched polyethers by ring-opening polymerization: Contribution of activated monomer mechanism, J. Polym. Sci. A Polym. Chem. 41 (2003) 457–468.
[60] H. Lian, S. Hong, A. Carranza, J.D. Mota-Morales, J.A. Pojman, Processing of lignin in urea–zinc chloride deep-eutectic solvent and its use as a filler in a phenol-formaldehyde resin, RSC Adv. 5 (2015) 28778–28785.
[61] O. Gordobil, R. Delucis, I. Egüés, J. Labidi, Kraft lignin as filler in PLA to improve ductility and thermal properties, Ind. Crop. Prod. 72 (2015) 46–53, https://doi.org/10.1016/J.INDCROP.2015.01.055.
[62] P.A. Sørensen, S. Kiil, K. Dam-Johansen, C.E. Weinell, Anticorrosive coatings: a review, J. Coat. Technol. Res. 6 (2009) 135–176.
[63] G.E. Spilman, A.W. Emerson, M. Beatty, M. Brown, M. Christy, J. Kovsky, K. Rogers, E. Vrabel, R. Tabor, Creating multifunctional coatings using recycled raw material streams, CoatingsTech 12 (2015).
[64] K. Crouvisier-Urion, P.R. Bodart, P. Winckler, J. Raya, R.D. Gougeon, P. Cayot, S. Domenek, F. Debeaufort, T. Karbowiak, Biobased composite films from chitosan and lignin: antioxidant activity related to structure and moisture, ACS Sustain. Chem. Eng. 4 (2016) 6371–6381.

[65] M.S. Bhalerao, A.V. Patwardhan, M.A. Bhosale, V.M. Kulkarni, B.M. Bhanage, Epoxidised soybean oil–Cu/Cu 2 O bio-nanocomposite material: synthesis and characterization with antibacterial activity, RSC Adv. 6 (2016) 38906–38912.
[66] S. You, Y. Xie, X. Zhuang, H. Chen, Y. Qin, J. Cao, T. Lan, Effect of high antioxidant activity on bacteriostasis of lignin from sugarcane bagasse, Biochem. Eng. J. 180 (2022) 108335.
[67] A. Cristoforetti, S. Rossi, F. Deflorian, M. Fedel, On the limits of the EIS low-frequency impedance modulus as a tool to describe the protection properties of organic coatings exposed to accelerated aging tests, Coatings 13 (2023) 598.